energies

MDPI

Article

Three-Dimensional Temperature Field Calculation and Analysis of an Axial-Radial Flux-Type Permanent Magnet Synchronous Motor

Dong Li [1,2,*], Yinghong Wen [1], Weili Li [2], Bo Feng [3] and Junci Cao [2]

1 School of Electronic and Information Engineering, Beijing Jiaotong University, Beijing 100044, China; yhwen@bjtu.edu.cn
2 School of Electrical Engineering, Beijing Jiaotong University, Beijing 100044, China; wlli@bjtu.edu.cn (W.L.); jccao@bjtu.edu.cn (J.C.)
3 Harbin Power System Engineering & Research Institute Co. Ltd., Harbin 150046, China; bof0302@163.com
* Correspondence: lidong223@bjtu.edu.cn; Tel.: +86-10-5168-5723

Received: 13 April 2018; Accepted: 7 May 2018; Published: 9 May 2018

Abstract: This article concentrates on the steady-state thermal characteristics of the Axial-Radial Flux-Type Permanent Magnet Synchronous Motor (ARFTPMSM). Firstly, the three-dimensional mathematical models for electromagnetic calculation and analyses are established, and the machine loss, including the stator loss, armature winding loss, rotor loss, and axial structure loss is calculated by using time-step Finite Element Method (FEM). Then, the loss distribution is assigned as the heat source for the thermal calculation. Secondly, the mathematical model for thermal calculation is also established. The assumptions and the boundary conditions are proposed to simplify the calculation and to improve convergence. Thirdly, the three-dimensional electromagnetic and thermal calculations of the machine, of which the armature winding and axial field winding are developed by using copper wires, are solved, from which the temperature distributions of the machine components are obtained. The experiments are carried out on the prototype with copper wires to validate the accuracy of the established models. Then, the temperature distributions of machine components under different Axial Magnetic Motive Force (AMMF) are investigated. Since the machine is finally developing by using HTS wires, the temperature distributions of machine developed by utilizing High Temperature Superconducting (HTS) wires, are also studied. The temperature distribution differences of the machine developed by using copper wires and HTS wires are drawn. All of these above will provide a helpful reference for the thermal calculation of the ARFTPMSM, as well as the design of the HTS coils and the cryogenic cooling system.

Keywords: axial-radial flux-type permanent magnet synchronous motor; steady-state temperature field; axial magnetic motive force; time-step Finite Element Method

1. Introduction

The High Temperature Superconducting (HTS) electric machines, of which the field windings or the armature windings are developed by utilizing the HTS wires, has advantages, such as higher power density, smaller volume, and less weight, etc. [1,2]. Therefore, it has been attracting worldwide attentions of the researchers. With the increase of the current-carrying capability and the critical properties, and the decrease of the construction cost, HTS wires or magnets are suitable to develop the high efficiency electric machines. Up to now, almost all types of HTS electric machines have been developed corresponding to the conventional machines [3–10]. However, we found that the researches on the HTS electric machines mainly focus on the electromagnetic calculations and the performance

investigations [11–13]. With the rapid development of the HTS electric machines, operation safety and stability become more and more important. The critical current of HTS windings is significantly influenced by the surrounding magnetic flux density and ambient temperature. If the HTS windings are used as the armature or field windings for electrical machines, the ac loss will generate within the HTS windings due to the ac current transportation. If the ac loss could not transfer to the ambient in time, the temperature of HTS windings will arise, and then the resistance of the HTS windings will increase due to the temperature rise. If this situation continues, the HTS windings may overheat or even quench [14,15]. Thus, it is vital to study the temperature distributions of the HTS electric machines.

Most of the literatures about the conventional electric machines are concentrated on the electromagnetic and thermal analyses [16–19], while for HTS electric machines, the literatures are mainly on the electromagnetic analysis or performance investigation [1,2,11,12], very few on thermal analysis. K. Sato et al. presented a nonlinear heat analysis technique, and by using the technique, he studied the temperature field of the 1000 MVA inner rotor superconducting generators [14]. P. J. Masson et al., utilize the thermal circuit method to establish the electro-thermal analysis model [7]. With the development of the computing technique, the Finite Element Method (FEM) could obtain more accurate results than the thermal circuit method [11]. Therefore, the FEM has been widely subjected to study the thermal field of the electric machines [11,12,17].

In the article, a new axial-radial flux-type permanent magnet synchronous motor is presented. Different from the conventional electric machines, the performance of Axial-Radial Flux-Type Permanent Magnet Synchronous Motor (ARFTPMSM) can be adjusted by changing Axial Magnetic Motive Force (AMMF). The three-dimensional steady-state temperature field distributions of ARFTPMSM under different AMMF are investigated by using time-stepping FEM. The comparisons of the temperature distributions between ARFTPMSM with copper wires and ARFTPMSM with HTS wires are conducted.

Although the ARFTPMSM is developed with copper windings, the structure is actually designed for ARFTPMSM with HTS windings. When compared with the conventional HTS electric machines, the ARFTPMSM with HTS windings has the following characteristics: firstly, the axial field windings and the radial field windings are both fixed on the stator. During operation, they do not rotate, thereby, the cryogenic cooling system would be simpler and more reliable. Secondly, the radial air-gap magnetic flux density could adjust by changing AMMF, thus, we can change the performance of ARFTPMSM by adjusting the AMMF, which differs from the conventional electric machines. Thirdly, the rated frequency of the machine is only 20.83 Hz, thus the ac loss of the HTS windings is very small and can even be ignored, so it can reduce the power of the cryogenic cooling system [20,21]. The total loss of the machine would be less than the machines that were developed by using the copper wires. Lastly, the rotor core is developed by using solid iron; thereby, the motor could be started up by itself [22,23].

The solid rotor core can increase the rotor loss and decrease the efficiency of the machine, but it has more merits than the lamination rotor core: (1) the machine with the solid rotor core can start up by itself, thus the converter can be saved. Therefore, the entire system of machine with solid rotor core is simpler, more reliable, and has higher efficiency; (2) Since the converter is saved, the machine can feed on ac source directly; the machine can operate with a good performance because of less current harmonics; (3) Each pole is composed of two radial magnets and two circumferential magnets, thus most parts of the rotor core are cut down for putting the magnets, so the solid rotor core has a higher strength than the lamination rotor core. Based on the analysis, the solid rotor core is used for the development of the prototype.

In order to investigate the influence of AMMF on the temperature distributions of the machine components, firstly the three-dimensional mathematical models for the electromagnetic field and temperature field calculations are established. When combined with the given boundary conditions, the electromagnetic model is solved by using the time-step FEM. The loss extracted from the electromagnetic calculations is then assigned as the heat sources for the thermal calculations. The three-dimensional steady-state temperature field calculation model is also established according

to the physical structure and the dimensions of the prototype, and then the temperature distributions of the machine components are studied separately. Then, the temperature field of ARFTPMSM under rated load are calculated, the results are compared with the experimental data to validate the accuracy of the established models. Then, the temperature field of ARFTPMSM under different AMMF are comparatively analyzed. Since the final goal is to develop ARFTPMSM with HTS wires, the temperature distributions of ARFTPMSM with HTS wires are also analyzed. The comparisons of the temperature distributions between the ARFTPMSM with copper wire and the ARFTPMSM with HTS wires are conducted. The contents in the paper can provide helpful guidelines for thermal design and temperature analyses of the axial-radial flux-type permanent magnet synchronous motor.

2. Heat Source Determination for Thermal Analysis

2.1. Physical Structure of ARFTPMSM

Figure 1 shows the basic physical structure of ARFTPMSM. The radial magnetic flux is provided by permanent magnets, while the axial magnetic flux is excited by the axial field windings. Both the armature windings and the axial field windings are developed by utilizing the copper wires. The machine is designed with 10 poles and 12 slots, thus, the armature windings can use the concentrate windings. So, it is suitable to develop machine with HTS windings. In order to provide more radial flux, each rotor pole is composed of two radial magnets and two circumferential magnets. Thus, most parts of the rotor core are cut out to put magnets. To strengthen the mechanical strength, the rotor core are fabricated by solid iron, while the stator core is constructed by silicon lamination sheets to reduce the core loss.

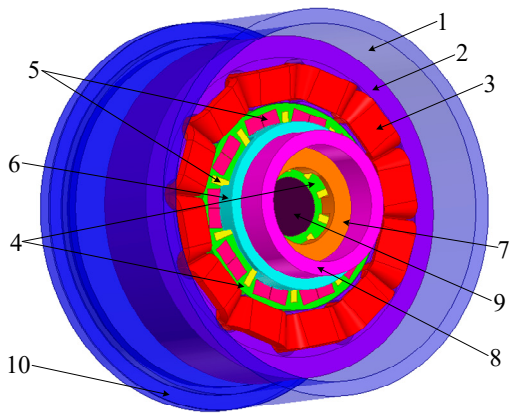

Figure 1. Physical structure of Axial-Radial Flux-Type Permanent Magnet Synchronous Motor (ARFTPMSM). 1-Enclosure, 2-Stator Core, 3-Armature Windings, 4-Rotor Core, 5-Permanent Magnets, 6-Outer Ferromagnetic Ring, 7-Inner Ferromagnetic Ring, 8-Axial Field Windings, 9-Shaft, 10-End Cover.

To save construction cost and to investigate the operating principles and performances of ARFTPMSM, a prototype, of which the armature windings and axial field windings are developed by utilizing copper wires, has been developed. The basic structure of the prototype is as shown in Figure 2 and the design parameters are listed in Table 1.

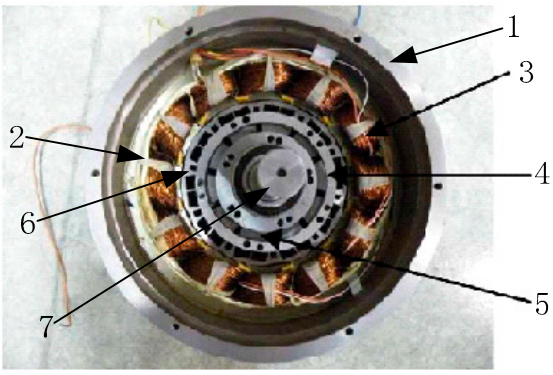

Figure 2. Basic structure of the prototype. 1-Enclosure, 2-Stator Core, 3-Armature Windings, 4-Outer Ferromagnetic Ring, 5-Inner Ferromagnetic Ring, 6-Rotor Core, 7-Shaft.

Table 1. Design parameters of the prototype.

Items	Value
Rated power/kW	3.5
Frequency/Hz	20.83
Synchronous speed/(r/min)	250
Core length/mm	50
Stator outer diameter/mm	230
Stator inner diameter/mm	140
Slots	12
Poles	10
Cooling type	Self-cooling

2.2. Mathematical Model for Electromagnetic Calculations

Due to the special structure of ARFTPMSM, the axial magnetic circuit is coupled with the radial magnetic circuit, and AMMF can change the radial flux density distributions of ARFTPMSM, thus, the loss calculations of ARFTPMSM is more complicated than the conventional machines. The loss of ARFTPMSM is composed of the armature winding loss, stator core loss, axial field windings loss, rotor core loss, and eddy current loss of permanent magnets and axial ferromagnetic rings. Because the stator core loss, the rotor core loss and eddy current loss of permanent magnets are hard to determine by using analytical method, thus, in the paper, we use the time-stepping FEM to calculate the loss of the machine. Due to the coupled magnetic circuits, 2d electromagnetic model could not satisfy the requirements for the loss calculation, therefore three-dimensional (3d) transient electromagnetic field model is established to consider the influence of AMMF. To simplify the electromagnetic calculation model and to save the calculation amount and time, the following assumptions are proposed [19,24]:

1. The current harmonics produced by the controller are ignored, so the machine is fed on ac source.
2. Because of the low frequency and the multi-strand windings, the displacement current within the armature windings is regardless.
3. According to the temperature measurements, the temperature rise of the machine is very small, thus, the influences of the temperature on material conductivity and permeability are ignored.
4. Since the end cover and the enclosure are developed by using high magnetic permeability materials, thus, the flux that is leaked into the air can be ignored.

The mathematical model described by using the magnetic vector potential A is established, as given in (1) [25].

$$\begin{cases} \Omega: \begin{cases} \frac{\partial}{\partial y}\left[\frac{1}{\mu}\left(\frac{\partial A_y}{\partial x}-\frac{\partial A_x}{\partial y}\right)\right]-\frac{\partial}{\partial z}\left[\frac{1}{\mu}\left(\frac{\partial A_x}{\partial z}-\frac{\partial A_z}{\partial x}\right)\right]=J_x-\sigma\frac{dA}{dt} \\ \frac{\partial}{\partial z}\left[\frac{1}{\mu}\left(\frac{\partial A_z}{\partial y}-\frac{\partial A_y}{\partial z}\right)\right]-\frac{\partial}{\partial x}\left[\frac{1}{\mu}\left(\frac{\partial A_y}{\partial x}-\frac{\partial A_x}{\partial y}\right)\right]=J_y-\sigma\frac{dA}{dt} \\ \frac{\partial}{\partial x}\left[\frac{1}{\mu}\left(\frac{\partial A_x}{\partial z}-\frac{\partial A_z}{\partial x}\right)\right]-\frac{\partial}{\partial y}\left[\frac{1}{\mu}\left(\frac{\partial A_z}{\partial y}-\frac{\partial A_y}{\partial z}\right)\right]=J_z-\sigma\frac{dA}{dt} \end{cases} \\ S: A=0 \end{cases} \tag{1}$$

where, $A = [A_x A_y A_z]^T$ is the magnetic vector potential, Ω is the solution domain, $J = [J_x J_y J_z]^T$ is the current density of the exciting source, the armature winding current and the axial field current included, S is the boundary of the solution domain, in this paper it is assigned to the enclosure and the end cover, μ is the permeability, and σ is the electrical conductivity.

According to the variation principle, the variation equation that is derived from (1) is given in (2).

$$\begin{cases} f(A)=\frac{1}{2}\iiint_\Omega \frac{1}{\mu}|rotA|^2 dv-\iiint_\Omega J\cdot A dv \\ n\times A|_s=0 \end{cases} \tag{2}$$

Equation (2) is discretized and solved by using Galerkin FEM. To fit the complicated physical structure of the machine, the tetrahedral elements are employed to mesh the solution domain. While the mesh process finalized, there are 142,204 tetrahedral elements within the solution domain. To obtain the electromagnetic field distribution, we should solve 217,669 matrix. The finalized mesh elements of partial machine are as shown in Figure 3.

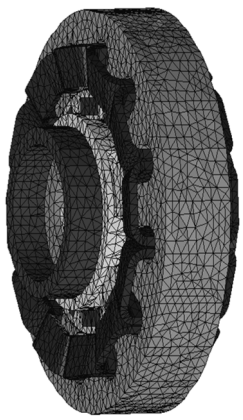

Figure 3. Partial mesh elements for the electromagnetic calculation.

During FEM calculations, the material properties of the components are set, as shown in Table 2. The remanence of permanent magnets is about 1.21 T at 20 °C, temperature coefficient is −0.095%/°C.

For soft magnetic materials, the core loss can be calculated by (3) [26,27].

$$\begin{aligned} P_{Fe} &= p_h(t)+p_c(t)+p_e(t) \\ &= k_h B^2 f + k_c (Bf)^2 + k_e (Bf)^{1.5} \end{aligned} \tag{3}$$

where: $p_h(t)$ is the static hysteresis loss, $p_c(t)$ is the classical eddy current loss, $p_e(t)$ is the additional loss. k_h, k_c, k_e are the coefficients of the loss, respectively; B is the flux density, and f is the frequency. The loss coefficients can be calculated by using the core loss curves at different frequency. In the paper, k_h, k_c, k_e are set as 0.0234 W/kg, 4.9068 W/kg, and 3.4328 W/kg, respectively. During calculations, the stack factor is set to 0.94 according the real prototype.

Table 2. Material properties for electromagnetic field analysis.

Items	Material	Relative Permeability	Bulk Conductivity
Stator core	DW310-35	Refer to Figure 4	0
Armature windings	Copper wire	1	5.91×10^7 S/m
Rotor core	DT-4	Refer to Figure 4	1.03×10^7 S/m
Permanent Magnets	N35EH	1.05	6.85×10^5 S/m
Outer Ferromagnetic Ring	DT-4	Refer to Figure 4	1.03×10^7 S/m
Inner Ferromagnetic Ring	DT-4	Refer to Figure 4	1.03×10^7 S/m
Axial Field Windings	Copper bar	1	5.91×10^7 S/m
Shaft	Steel 45	Refer to Figure 4	2.0×10^7 S/m
Enclosure	Steel 45	Refer to Figure 4	2.0×10^7 S/m
End Cover	Steel 45	Refer to Figure 4	2.0×10^7 S/m

The magnetizing characteristics of soft magnetic materials used in the prototype are as shown in Figure 4. From which, it can observe that the electrical iron DT-4 have the great magnetic permeability as DW310-35 silicon lamination sheets, while the steel 45 shows poor magnetic permeability by comparing it with DW310-35 and DT-4. However, it is used to fabricate the shaft, end cover, and enclosure because of the low cost. All of the materials refers to Chinese standard of materials.

As stated above, the rotor core is fabricated by using the solid electrical iron, the eddy current loss component of the solid rotor core is calculated in a transient FEM simulation by referring to the corresponding material conductivity. The other loss components of the solid core are post-processed through the built-in Bertotti equation in the FEM software. The corresponding coefficients refer to [28], where the k_h and k_e are 496.5 $\mathrm{WsT^{-2}m^{-3}}$ and 0, other quantities refer to the material properties. Extracted from FEM simulation, the eddy current loss is about 14.8 W while the hysteresis loss is only 0.024 W, thus the hysteresis loss is neglected during the rotor loss calculations.

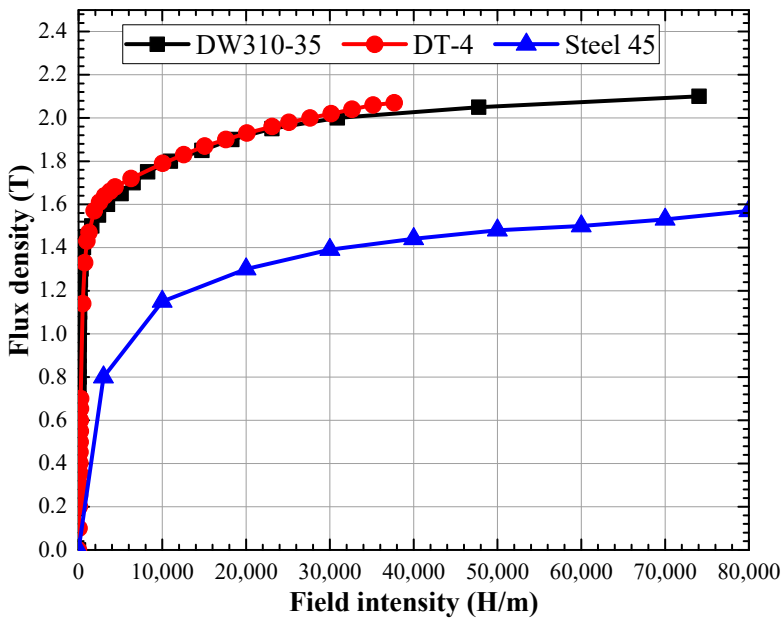

Figure 4. Magnetizing curves of the ferromagnetic materials.

Based on the analysis above, the electromagnetic field is calculated and the mainly loss obtained from FEM simulations are as shown in Table 3. The winding loss includes the armature winding loss and the axial field winding loss. The rotor loss is composed of the rotor core loss and the eddy current loss of permanent magnets. The axial field loss is composed of two parts: dc resistance loss and eddy

current loss. Since the axial field windings are fed on dc supply, thus, the ferromagnetic ring loss is mainly sourced from the end edge leakage flux.

Table 3. Main Loss in the Prototype.

Items	Value
Stator core loss	1.96 W
windings loss	17.4 W
Ferromagnetic rings loss	0.76 W
Rotor loss	14.8 W

3. Mathematical Model for Thermal Calculation

3.1. Assumptions and Boundary Conditions

The presented prototype is a fully enclosed self-cooling machine, thus, the temperature distributions are highly related to the loss distributions. Due to the special structure, the 3d mathematical model is necessary for the thermal calculation. According to heat transfer theories and the physical structure of the machine, 3d steady-state temperature field calculation model are set up as shown in Figure 5. All of the components are constructed corresponding to the real structure and the dimensions of the prototype. To save the computations and time, the following assumptions are proposed to simplify the calculations [29,30].

1. Since the rotor core is developed by using solid iron, the eddy loss is distributed with a certain thickness according to the skin effect. So, when considering the real state of the loss distributions, the eddy current loss of the rotor core is distributed within a certain penetration depth of the rotor core.
2. During the loss calculations, the temperature effect on the material properties are ignored, thus, the influence of the temperature on the heat transfer is regardless.
3. Due to the low rotating speed and totally enclosed structure, the influence of the flowing air within the machine on the heat transfer is also ignored.
4. During the assembly process, the machine is vacuum-dipped to evacuate the air within the connect joints, so it regards that there is no air-gap between the connection joints.

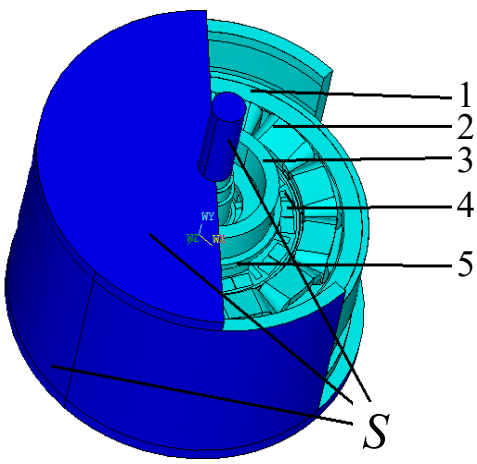

Figure 5. Three-dimensional (3d) steady-state temperature field calculation model. 1-Stator Core, 2-Armature Windings, 3-Axial Field Windings, 4-Permanent Magnets, 5-Ferromagnetic Ring, *S*-Boundary for Thermal Calculations.

According to thermodynamics principles, 3d steady-state temperature field mathematical model and its boundary conditions are described in (4) [18,24]:

$$\begin{cases} \Omega : \frac{\partial}{\partial x}\left(\lambda_x \frac{\partial T}{\partial x}\right) + \frac{\partial}{\partial y}\left(\lambda_y \frac{\partial T}{\partial y}\right) + \frac{\partial}{\partial z}\left(\lambda_z \frac{\partial T}{\partial z}\right) = -q(x,y,z) \\ S : -\lambda \frac{\partial T}{\partial n} = \alpha\left(T - T_f\right) \end{cases} \tag{4}$$

where T is the temperature in the solution domain, λ_x, λ_y, λ_z are the thermal conductivity along x-axis, y-axis, and z-axis, respectively, q is the heat flux, n is the normal vector of the boundary surface S, α is the heat transfer coefficient, T_f is ambient temperature, and S is the outer surface of the enclosure and end cover (as shown in Figure 5).

Similar to the electromagnetic calculation, the Equation (3) could also discretize and solve by using FEM. Different with the electromagnetic model, the thermal model is meshed according to the component structure, e.g., The stator and rotor cores are meshed with triangular or quadrangular prism elements, while the armature windings and the axial field windings are meshed by using the sweep method with quadrangular prism elements, etc. while the mesh process is finalized, there are total 86,735 elements with 235,505 nodes for the entire models.

3.2. Thermal Conductivity of Air-Gap

The thermal conductivity of the air between the static parts and the movable parts changes with the rotating speed. To stress the influence of the rotating speed on the thermal conductivity, we consider using the equivalent thermal conductivity of the static air to account for the effect of rotating speed on the thermal conductivity. In ARFTPMSM, the air-gap includes the normal air-gap between the stator and rotor, as shown in Figure 6a, and the axial air-gap between the axial field windings and the ferromagnetic rings, as shown in Figure 6b. The thermal conductivity of the normal air gap and axial air gap should be treated separately, due to the different structures.

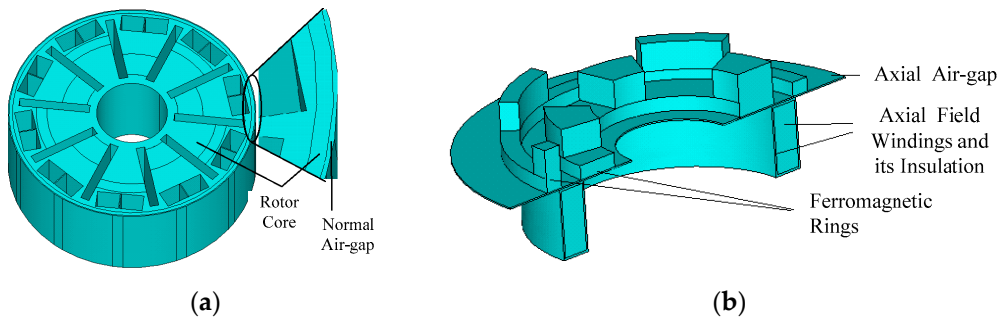

Figure 6. Schematic diagram of air-gap of the machine, (**a**) normal air-gap; and, (**b**) axial air-gap.

3.2.1. Thermal Conductivity of Normal Air-Gap

Figure 6a shows the schematic diagram of the normal air-gap. The rotation of the rotor drives the air in the normal air-gap to spin. Thus, the thermal conductivity will influence by the flowing state of the air in the air gap. To simplify the calculation, the equivalent thermal conductivity λ_r is introduced to represent the heat exchange capacity of the rotating air in the normal air-gap. By this way, the rotating air could be equivalent to the static air. The equivalent thermal conductivity could be determined, as follows [24,30]:

The Reynolds number R_a in the normal air-gap is calculated by (5).

$$R_a = \pi D_2 g \frac{n}{60\gamma} \tag{5}$$

where D_2 is the outer diameter of the rotor, m; g is the normal air-gap length, m; n is the motor speed, r/min; and, γ is the kinematic viscosity of air, m^2/s.

The critical Reynolds number R_{cr} is given by (6).

$$R_{cr} = 41.2\sqrt{\frac{D_{i1}}{g}} \tag{6}$$

where D_{i1} is the inner diameter of the stator, m.

If $R_a < R_{cr}$, the air flowing in the air-gap is laminar, the heat dissipation of the air-gap is independent of the rotation of the rotor, the heat transfer form in air-gap is heat conduction, and the equivalent thermal conductivity λ_n equals to static air heat conductivity λ_{air}; however, if $R_a > R_{cr}$, then the air flow in the air-gap is turbulent, and the equivalent thermal conductivity λ_n is determined by (7) [31,32].

$$\begin{cases} \lambda_n = 0.069\eta^{-2.9048} R_a{}^{0.4614\ln(3.33361\eta)} \\ \eta = \frac{D_2}{D_{i1}} \end{cases} \tag{7}$$

3.2.2. Thermal Conductivity of Axial Air-Gap

Figure 6b shows the schematic diagram of the axial air-gap. The rotation of the rotor also drives the air in the axial air-gap to spin. For the smooth end surface of the axial field windings and the ferromagnetic rings, theReynolds number of the axial air-gap is less than the critical Reynolds number. So, the equivalent thermal conductivity λ_a equals to the air heat conductivity λ_{air}.

3.3. Heat Transfer Coefficient of the Enclosure

The heat transfer coefficient α of the enclosure could be determined, as follows [33]:

$$\alpha = 14(1 + 0.5\sqrt{\omega_i}) \sqrt[3]{\left(\frac{\theta}{25}\right)} \tag{8}$$

where, ω_i is wind velocity blowing to the surface of the enclosure; and, θ is the enclosure temperature.

Due to the fully enclosed self-cooling structure and the low speed of the machine, the influence of the flowing air going through the outer surface of the machine on the heat transfer coefficient could be ignored. So, the heat transfer coefficient of the enclosure could be calculated by (9).

$$\alpha = 14 \sqrt[3]{\left(\frac{\theta}{25}\right)} \tag{9}$$

In this paper, the machine is tested indoor with no wind, and the ambient temperature is 22 °C. The heat transfer coefficient that was obtained from (9) is 31.8 W/(m^2 K).

3.4. Thermal Conductivity of Armature Windings

Before the thermal calculations, the thermal conductivity of the armature windings should be determined due to the anisotropic properties caused by the wire package. As shown in Figure 7a, the real armature windings is made up by using multi-strand copper wires, and each strand of the wire are insulated by using the wire package. To simplify the calculation model, we use the equivalent winding, as shown in Figure 4b, to replace the multi-strand copper wires. During the equivalent process, the equivalent winding has the same heat transfer capacity as the real multi-strand copper

wires. Then, the equivalent thermal conductivity of the armature windings can be determined by the equations below [34].

$$\lambda' = \frac{S}{\frac{S_{cu}}{\lambda_{cu}} + \frac{S_{in}}{\lambda_{in}}} \tag{10}$$

where, λ', λ_{cu}, and λ_{in} are the equivalent thermal conductivity of the equivalent winding, copper wire, and the wire package, respectively. S, S_{cu}, and S_{in} are the areas that are occupied by the equivalent winding, the copper wire, and the wire package, respectively.

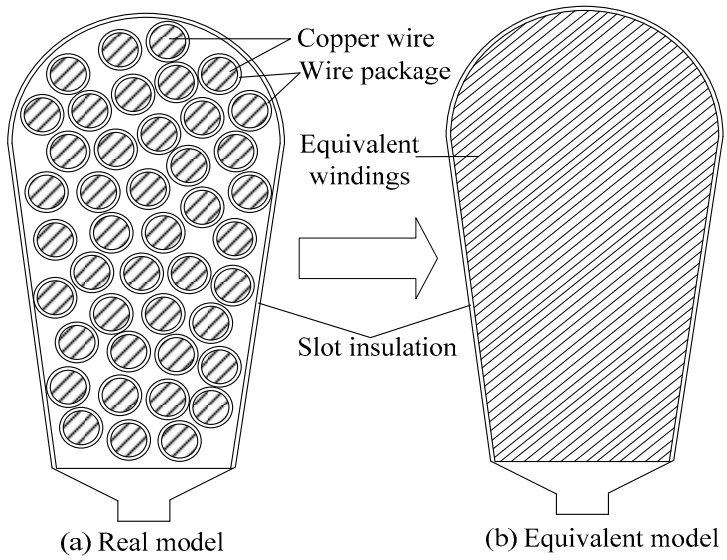

Figure 7. Equivalent model of the armature windings in one slot, (**a**) real model of windings in stator slot; and, (**b**) equivalent model of windings in stator slot.

Based on the analysis above, the material properties for thermal field analysis are summarized in Table 4. From which, it can be obtained that the thermal conductivity of stator core is anisotropic. When comparing the armature windings with the axial field windings, the thermal conductivity of armature windings is far lower than the axial field windings.

Table 4. Material properties for thermal field analysis.

Items	Mass Density	Specific Heat Capacity	Thermal Conductivity
Stator core	7600 kg/m^3	470 J/(kg K)	43 W/(m K) in x,y-axis 0.62 W/(m K) in z-axis
Armature windings	8900 kg/m^3	504 J/(kg K)	1.7 W/(m K)
Slot insulation	1020 kg/m^3	1000 J/(kg K)	0.23 W/(m K)
Slot wedge	900 kg/m^3	800 J/(kg K)	0.25 W/(m K)
Normal air-gap	1.2 kg/m^3	1005 J/(kg K)	0.045 W/(m K)
Permanent magnets	7600 kg/m^3	502 J/(kg K)	12 W/(m K)
Rotor core	7870 kg/m^3	460J J/(kg K)	48 W/(m K)
Shaft	7850 kg/m^3	472 J/(kg K)	49.8 W/(m K)
Enclosure & end cover	7850 kg/m^3	472 J/(kg K)	49.8 W/(m K)
Axial field windings	8900 kg/m^3	504 J/(kg K)	398 W/(m K)
Axial ferromagnetic rings	7870 kg/m^3	460 J/(kg K)	48 W/(m K)
Axial air gap	1.2 kg/m^3	1005 J/(kg K)	0.045 W/(m K)

4. Steady-State Temperature Field Calculation for Prototype

4.1. Verification for Mathematical Models

Based on the established models and material properties, 3d temperature field mathematical model of the prototype operating at a rated torque of 8.6 N m and 0 Ampere-turn (At) AMMF is solved. Then, the temperature distributions of the machine can be obtained, as shown in Figure 8. Observed from Figure 8, the max temperature is about 52.54 °C, located on the armature windings, while the min temperature is 32.04 °C, located on the enclosure. Whenn compared with the ambient temperature, the rated temperature rise is 29.54 K.

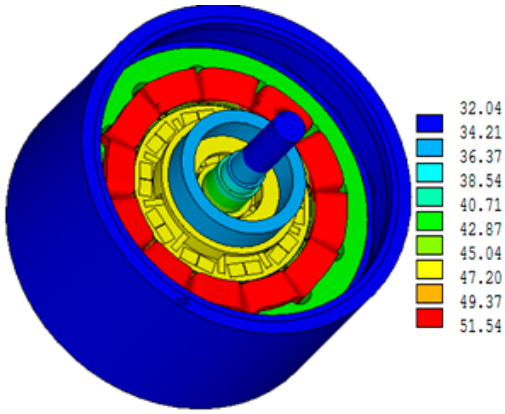

Figure 8. 3d temperature distributions of machine operating at rated torque of 8.6 N m and 0 At Axial Magnetic Motive Force (AMMF) (°C).

To validate the accuracy of the established electromagnetic and the thermal field mathematical models, the temperature experiments have carried out on the prototype under rated load and 0 At AMMF. The temperature probes (Pt 1000) are fixed on the end of the armature windings and the outer surface of the enclosure. During the test process, we can record the resistance of the temperature probes by using the resistance measurement instrument. Then, we can obtain the temperature by referring to the given temperature-resistance tables. By this measurement method, the precision can keep within 0.1 °C. During temperature measurement, the resistance data is recorded every 5 min. When the temperature between two measured points are within 0.1 °C, it can regard that the machine reaches up to a thermal steady state.

Table 5 shows the comparison of the calculation results and measurements. From which, we could get that the temperature difference between the calculation results and the measurements of the end radial armature windings is 1.05 °C While the temperature difference between the calculation and the measurement results of the enclosure is 0.96 °C, both of the errors are less than 5%, it could satisfy the requirements in engineering. The differences between the calculation results and measurements are so small, and it can prove that the electromagnetic and thermal calculation models for the machine is accurate enough for the electromagnetic field and thermal field analyses.

Table 5. Comparison of Calculation Results with Measurements under rated torque and 0 At AMMF.

Items	Calculation Results	Measurements	Error (%)
End armature windings/°C	51.15	50.10	2.10%
Enclosure/°C	32.04	33.00	−2.91%

4.2. Temperature Field under Different AMMF

The 3d temperature field mathematical models of the machine under 0 At, 600 At, and 900 At AMMF are calculated to investigate the influence of AMMF on the temperature distribution of the machine. During the calculations, the load torque is still kept at 8.6 N m. The calculation results are compared, as shown in Table 6. From which, one can obtain that the temperature of the end armature windings and the enclosure increases as AMMF increases. The enclosure temperature increases faster than the temperature of the end armature windings. The reason can be explained that, as AMMF increases, the axial field winding loss increases dramatically, the axial air gap can prevent the heat transfer from the axial field windings to stator and rotor cores because of the poor thermal conductivity of the axial air-gap. Therefore, the heat that is generated in the axial field windings can only transfer to armature windings by through the ferromagnetic ring and end cover. In addition, the increase of AMMF can also made the harmonic components of the air gap flux density arise, which will also can increase the rotor loss. All of these above made the temperature increase significantly as AMMF increases.

Table 6. Calculation Temperature of machine components under Different AMMF.

AMMF/AT	End Armature Windings/°C	Enclosure/°C
0	51.15	32.0
600	54.7	36.8
900	60.9	52.8

Because the temperature limitation of components is different, the temperature distribution of the machine components should be studied separately.

4.2.1. Thermal Analysis for the Rotor Components

The remanence of the permanent magnets may demagnetize as the temperature increases. The rotor core is built by using solid iron, it has larger loss than the silicon lamination sheets. The permanent magnets are encompassed by the rotor core, therefore, the temperature distributions of the rotor core are studied firstly. The obtained temperature distribution of the rotor core is as shown in Figure 9. The temperature of the middle parts of the rotor core is higher than the temperature of the normal air gap and the shaft. It indicates that the heat generated in the rotor core is transferred to ambient by two ways: one is going from the air gap to stator core and another is going from the ambient by through the shaft. When compared with the machine with 0 At AMMF, the max temperature of the rotor core of the machine under 600 At and 900 At AMMF increases by about 4.09 °C and 12.42 °C, respectively. As AMMF increases, the temperature distributes more evenly, because the heat transfer capacity of the shaft is very small. As the loss increases, the shaft can not transfer all of the loss to the ambient through the shaft.

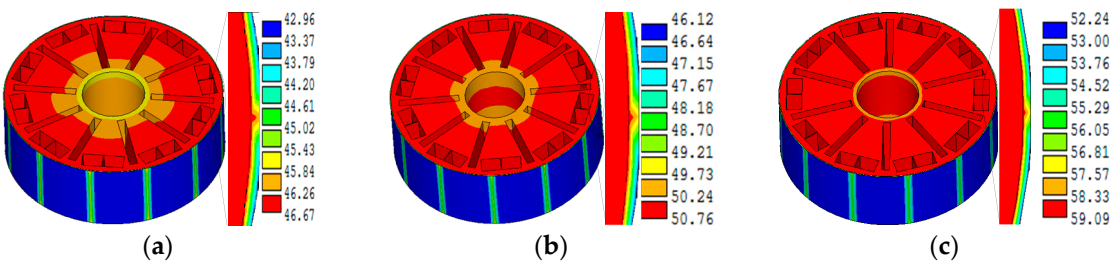

Figure 9. Temperature distribution of the rotor core under different AMMF (°C); (**a**) 0 At AMMF; (**b**) 600 At AMMF; and, (**c**) 900 At AMMF.

The temperature distributions of the permanent magnets are as shown in Figure 10. The max temperature located on the outer surface of the circumferential magnets while the min temperature is on the inner surface of the radial magnets. The temperature decrease along the radial direction, which also confirms that the shaft can transfer the heat to the ambient. The temperature differences between the max and the min temperature under 0 At, 600 At, and 900 At is 0.82 °C, 0.76 °C, and 0.69 °C, respectively. In addition, when we compare Figure 9 with Figure 10, the max temperature of the permanent magnets equals to the temperature of the rotor core at all occasions. It is because the permanent magnet loss is far less than the rotor core loss. Therefore, the temperature distribution of permanent magnets is actually determined by the temperature field of the rotor core.

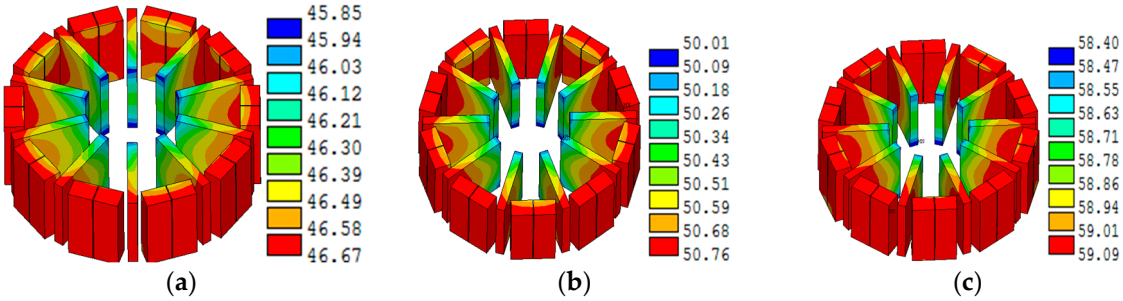

Figure 10. Temperature distributions of the permanent magnets under different AMMF (°C); (**a**) 0 At AMMF; (**b**) 600 At AMMF; (**c**) 900 At AMMF.

4.2.2. Thermal Analysis for the Stator Components

The basic structure of the stator is as shown in Figure 11. The stator is composed of the stator core and armature windings. The temperature distributions of the stator are as shown in Figure 12. The max temperature of the stator located on the armature windings while the min temperature is on the outer surface of the stator core. Because of the poor heat transfer capacity of the slot insulation and slot wedge, they construct a thermal barrier to prevent the heat transferring to the stator core. Thus, there is obvious temperature difference between the armature windings and the stator core.

The max temperature of the stator core locates on the tooth top; therefore, the temperature variations on the stator core tooth top are also studied as shown in Figure 13. The position on the stator core tooth top is as shown in Figure 11. From which one can observe that the temperature from position a to position b decreases firstly and then increases, from position b to position c, it shows the similar variation trend with that from position a to position b. it is determined by the physical structure of the stator core tooth top. In addition, the temperature of the stator core tooth increases as the AMMF as well.

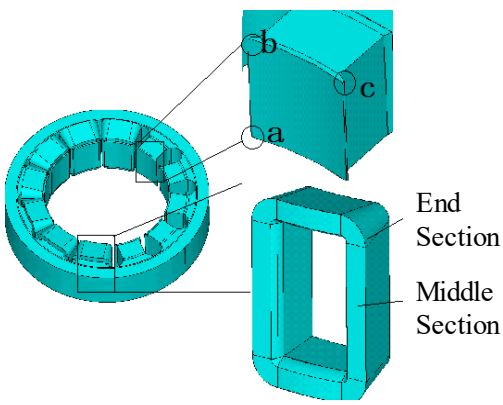

Figure 11. Schematic diagram of the stator components.

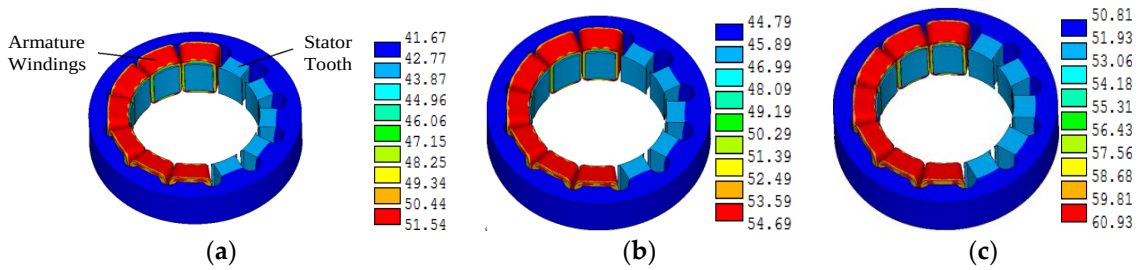

Figure 12. Temperature distributions of the stator (°C); (**a**) AMMF 0 AT; (**b**) AMMF 600 AT; and, (**c**) AMMF 900 AT.

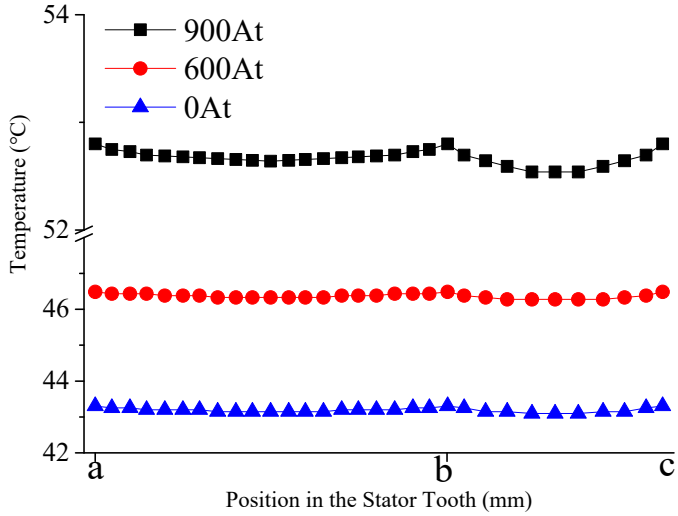

Figure 13. Temperature variations of the stator core tooth top under different AMMF.

Figure 14 shows temperature distributions of the armature windings under different AMMF. From which, one can observe that the temperature on the end windings are higher than the middle part. While AMMF increases from 0 At to 600 At, the max and min temperature increases by 3.15 °C and 3.12 °C, respectively. The average temperature increases about 6.9%. However, while AMMF rises from 600 At to 900 At, the max and min temperature increases by 6.24 °C and 6.83 °C The average temperature increases by about 15.2%. The variation trend is nonlinear. Thus, it should pay more attention to the adjustment of the axial field current.

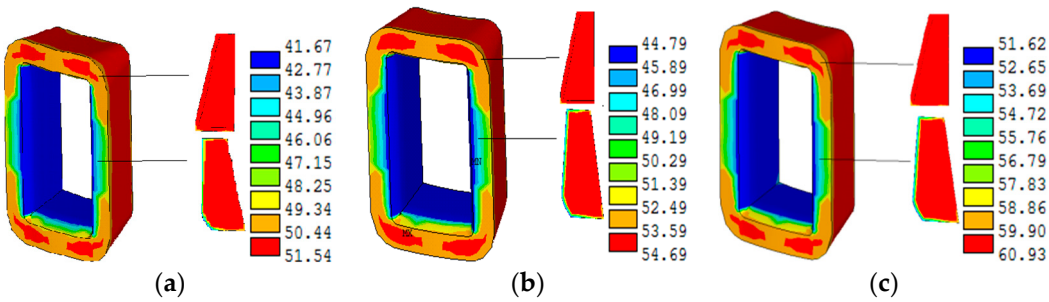

Figure 14. Temperature distributions of the armature windings under different AMMF (°C); (**a**) 0 At AMMF; (**b**) 600 At AMMF; and, (**c**) 900 At AMMF.

4.2.3. Thermal Analysis for Axial Field Structure

The axial field structure consists of the axial field windings, axial air-gap, and the ferromagnetic rings. Figure 15a,b show the cross-section of the tooth and slot of the outer ferromagnetic ring, respectively. The temperature distributions on the cross-section are as shown in Figure 16. As observed from Figure 16, it can be seen that the temperature of the field windings increases significantly as AMMF increases. It is because that the axial field winding loss increases quickly as AMMF. From the enlarge view of the temperature distribution of the axial field windings (as shown in Figure 16a), it is clear that the heat conducts from the ferromagnetic rings to the axial windings through the axial air-gap. When compared with Figure 16a,b, it shows that the temperature of the axial field windings is lower than the ferromagnetic rings, thus the heat will transfer from the ferromagnetic rings to the axial field windings. However, viewed from Figure 16c, the temperature of the field windings are larger than the ferromagnetic rings, it would cause the heat transfer direction reverse by comparing with Figure 16a,b.

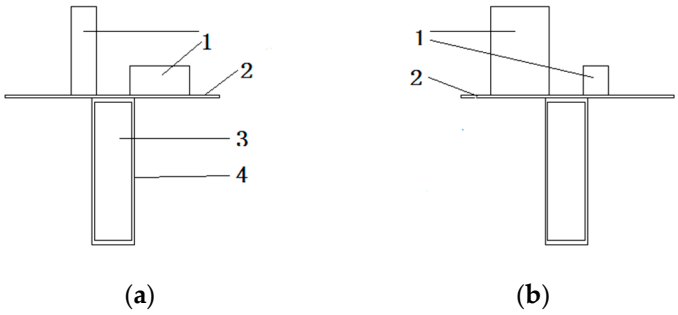

Figure 15. Cross-section for the axial field structure. 1-ferromagnetic rings, 2-axial air-gap, 3-axial field winding, 4-electrical insulation; (**a**) left section of the axial field structure; and, (**b**) right section of the axial field structure.

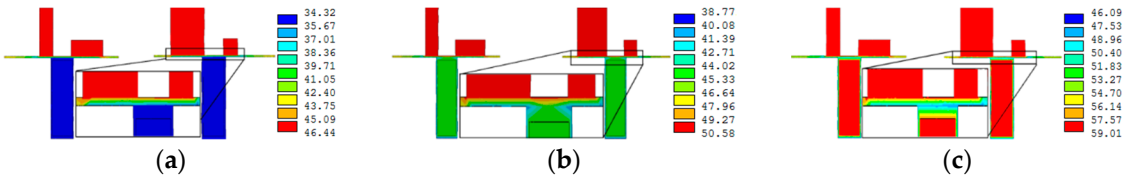

Figure 16. Temperature distributions of the axial field structure under different AMMF (°C); (**a**) 0At AMMF; (**b**) 600 At AMMF; and, (**c**) 900 At AMMF.

5. Temperature Field for ARFTPMSM with HTS Windings

Since the final goal is to develop an ARFTPMSM with HTS windings, thus we should investigate the temperature field firstly. So, it can provide us guides for the construction of the HTS machine. Once the axial field windings and armature windings are developed by using HTS wires, the loss of the armature windings and the axial windings are very small, so they could be ignored. The heat transfer process may differ from the ARFTPMSM with copper wires. In order to compare with the prototype, we continue to use the model and thr material properties for original prototype. Therefore, the difference between the HTS motor and the copper motor is only caused by the windings loss.

5.1. Temperature Field for the Rotor Components

Firstly, the temperature distribution of the rotor core is studied. When compared with Figure 17a–c, we could obtain that: (1) the max temperature located in the rotor core, whereas the min temperature is on the normal air-gap. (2) The max temperature and the min temperature under 600 At is less than that under 0 At and 900 At. What we observed could be explained as follows. While AMMF increases

from 0 At to 600 At, the axial flux reinforces the normal air-gap flux. Thus, it needs less armature current in order to produce the same torque. Thus, the small armature current will produce small rotor loss. Then, the corresponding temperature will also decrease. As the increase of the AMMF continues, the axial flux would weaken the normal air-gap magnetic flux, there need larger armature current to produce the same torque. Thus, the corresponding temperature increases. In addition, since the loss of axial field winding and armature winding is very small, the entire temperature decreases, when comparing with the temperature distributions of the machine with copper wires.

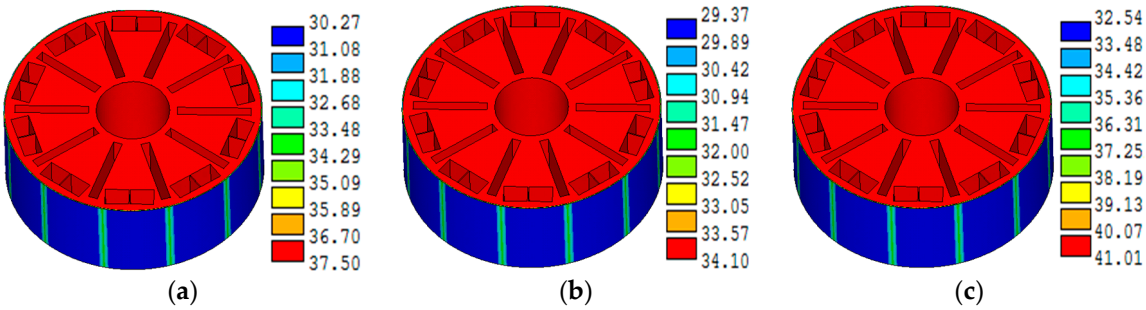

Figure 17. Temperature distribution of the rotor core (°C); (**a**) 0 At AMMF; (**b**) 600 At AMMF; and, (**c**) 900 At AMMF.

The temperature distributions of the permanent magnets under different AMMF are as shown in Figure 18. The temperature differences between the max and the min temperature are 0.51 °C, 0.34 °C, and 0.54 °C, respectively, which are still less than 1 °C The max temperature locates on the inner surface of the circumferential and radial magnets, especially concentrates on the connection joint with the rotor core, it is very different with the temperature distributions of the permanent magnets with copper wires. It indicates that the rotor core loss is larger than the permanent magnet loss, and the heat of the rotor core transfers to the permanents.

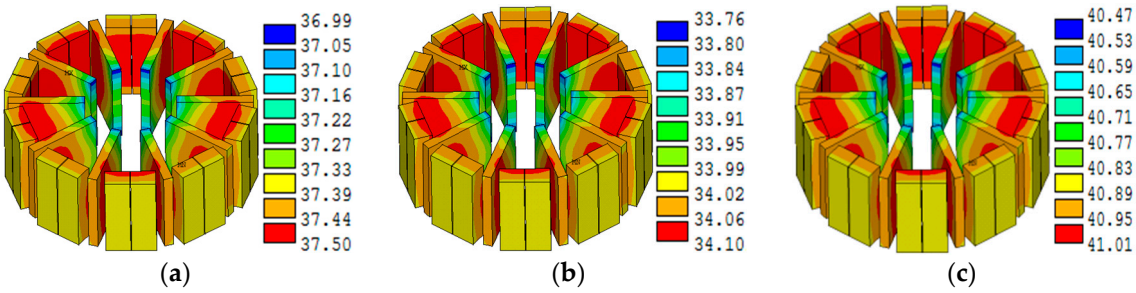

Figure 18. Temperature distribution of the permanent magnets under different AMMF (°C); (**a**) 0 At AMMF; (**b**) 600 At AMMF; and, (**c**) 900 At AMMF.

Figure 19 compares the rotor core temperature of the machine that was developed by using copper wires and HTS wires. From which, the following results could be obtained: the rotor core temperature of the machine with copper wires increases with the increase of the AMMF; however, the rotor core temperature of the machine with HTS wires decreases firstly, and then increases as AMMF increases. It could be explained that for machine with copper wires, although the axial field flux can adjust the normal air gap flux, the change of the normal air gap flux has little influence on the rotor loss. Since the loss of armature winding and the axial field winding is too large, the temperature is still determined by the armature winding and axial field winding. However, for the machine with HTS wires, the loss of armature winding and axial field loss is ignored, thus, the temperature distributions is manly determined by the stator core loss and rotor loss. From the electromagnetic calculations,

we know that the rotor loss is far larger than the stator core loss. Thus, the temperature distributions of the rotor are determined by the rotor loss. Thus, the little change of the rotor loss will reflect on the rotor temperature distributions. When AMMF increases from 0 At to 600 At, the max and min temperature of rotor core decreases by about 8.84% and 2.87%, respectively; however, while comparing temperature of rotor core of the machine with HTS wires under 900 At with that under 0 At, the max and min temperature of rotor core increases by about 8.84% and 8.05%, respectively. While under 600 At AMMF, the max rotor temperature of machine with copper wires is about 47.96% larger than that of the machine with HTS wires.

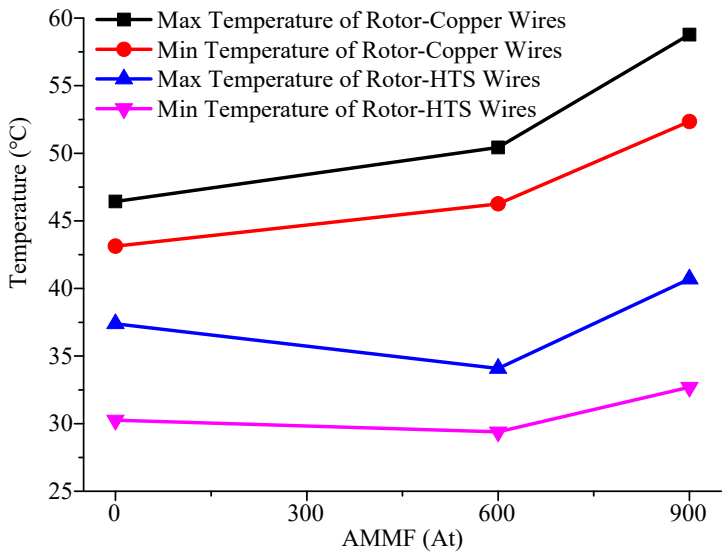

Figure 19. Comparisons of the rotor core temperature of the machine developed by using copper wires and High Temperature Superconducting (HTS) wires.

5.2. Temperature Field for the Stator

Figure 20 describes the stator temperature of the machine with HTS wires. From which, we can observe that the temperature decreases from the stator core tooth top to the outer surface of the back of the stator core. The temperature of the armature windings also decreases along the radial direction. It indicates that the heat transfer path goes from the rotor core to the enclosure by through the normal air-gap and the stator core. When compared with the machine operating at 0At AMMF, the max stator temperature of the machine under 600 At and 900 At decreases by about 2.93% and increases 16.22%, respectively.

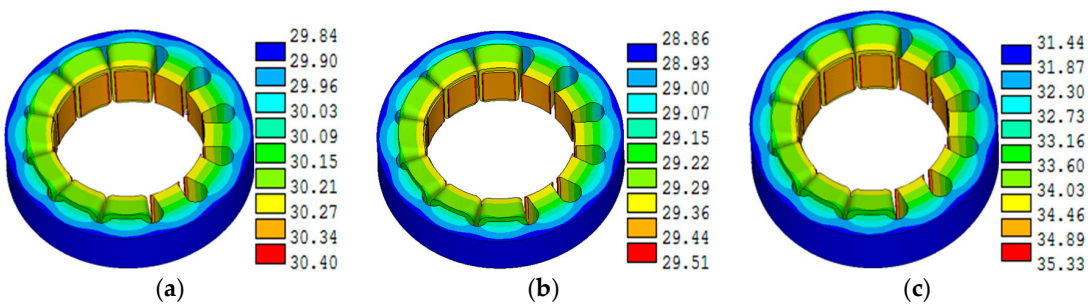

Figure 20. Stator temperature distribution of the machine with HTS wires (°C); (**a**) 0 At AMMF; (**b**) 600 At AMMF; and, (**c**) 900 At AMMF.

Stator temperature of the machine that was developed by copper wires and HTS wires is described, as shown in Figure 21. For the machine with copper wires, the differences between the max and min stator temperature under 0 At, 600 At, and 900 At are 9.57 °C, 9.57 °C, and 9.74 °C, respectively. The temperature gradient of the stator do not change as AMMF increases. However, for the machine with HTS wires, the differences between max and min stator temperature under 0 At, 600 At, and 900 At are 0.35 °C, 1.04 °C, and 4 °C, respectively. The temperature gradient increases with AMMF.

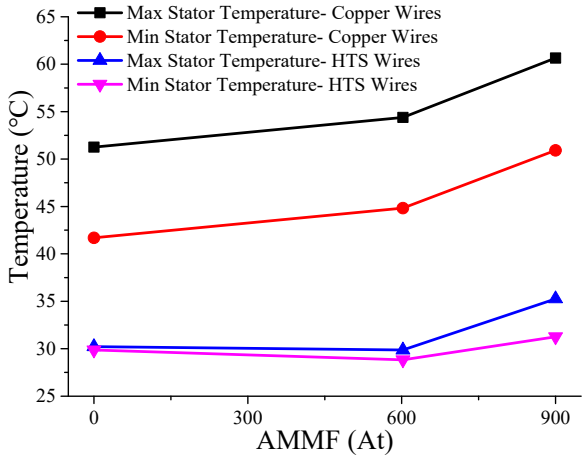

Figure 21. Comparisons of the stator temperature of the machine developed by copper wires and HTS wires.

5.3. Temperature Field for the Axial Field Structure

Since the axial field windings are excited by the dc source, if the axial field windings developed by HTS wires, the axial field windings loss could be negligible. Thus, the loss of the ferromagnetic rings is the only heat source of the axial field structure. Figure 22 shows the temperature field of the axial field structure under different AMMF. From which, we can obtain that the max temperature under different AMMF are all located on the ferromagnetic rings, however the min temperature is with the min temperature. The heat transfer path goes from the ferromagnetic rings to the axial field windings through the axial air gap.

Figure 23 compares the axial field structure temperature of the machine developed by copper wires and HTS wires. For the machine with copper wires, the differences between the max and min temperature of the axial field structure are 11.87 °C, 4.41 °C, and 10.8 °C, respectively. The temperature gradient of the axial field structure can be adjusted by changing AMMF. However, for the machine with HTS wires, the differences of the max and min temperature of the axial field windings are 8.98 °C, 6.63 °C, and 11.72 °C, respectively. It indicates that the influence of the axial field winding loss on the temperature gradient is very small.

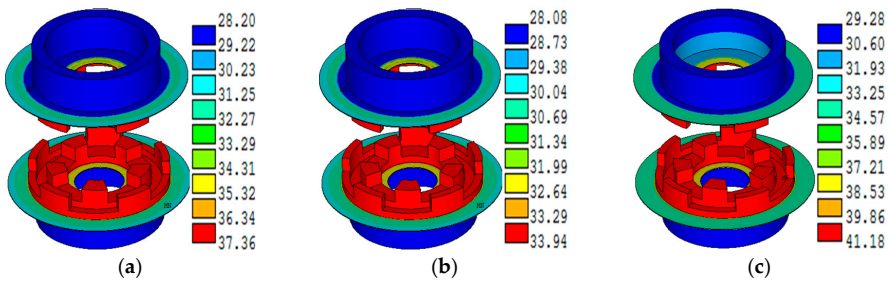

Figure 22. Temperature distribution of the axial field structure under different AMMF (°C); (**a**) 0 At AMMF; (**b**) 600 At AMMF; and, (**c**) 900 At AMMF.

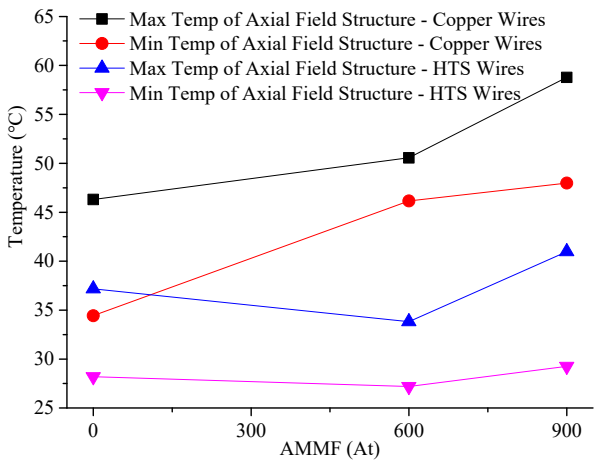

Figure 23. Comparisons of the axial field structure temperature of the machine developed by copper wires and HTS wires.

6. Conclusions

In this article, a new axial-radial flux-type permanent magnet synchronous motor is presented; the normal air gap flux can be adjusted by changing the axial magnetic motive force. Firstly, the temperature distribution of machine components under different AMMF are investigated, and then while considering the HTS applications, the temperature distributions of the machine that was developed by using copper wires and HTS wires are also comparatively analyzed. Based on the analyses, the following conclusions can be obtained:

1. Validated by the experiments carried out on the prototype, the differences between the calculations and the measurements of the end armature temperature and enclosure are 1.05 °C and 0.96 °C, respectively. It indicates that the established models and the presented assumptions are reasonable for the thermal analysis of ARFTPMSM.
2. For machine with copper wires, although AMMF can adjust the normal air gap flux density, but it can also increase the harmonic components of the normal air gap flux density. Thus, the temperature of machine components increases as AMMF increases, e.g., the max temperature of the rotor core of the machine under 600 At and 900 At AMMF increases by about 4.09 °C and 12.42 °C, respectively, while when compared with the machine with 0 At AMMF. While AMMF rises from 0 At to 600 At, the average temperature of armature windings increases about 6.9%; however, while AMMF rises from 600 At to 900 At, the average temperature increases about 15.2%.
3. While the machine is developed by HTS wires, the temperature distribution is quite difference with the machine with copper wires. Viewing from the temperature distribution of rotor, the max rotor temperature of machine with copper wires is about 47.96% larger than that of the machine with HTS wires that are under 600 At AMMF.
4. For the machine with copper wires, the differences between the max and min stator temperature under 0 At, 600 At, and 900 At are 9.57 °C, 9.57 °C, and 9.74 °C, respectively. The temperature gradient do not change as AMMF increases. However, for a machine with HTS wires, the differences between max and min stator temperature under 0 At, 600 At, and 900 At are 0.35 °C, 1.04 °C, and 4 °C, respectively. The temperature gradient increases as AMMF.

Author Contributions: D.L. has done the electromagnetic and thermal analyses and supervised the entire process for the paper, Y.W. provides the analysis method for the axial field magnetic motive force, W.L. provides the thermal calculation method. B.F. has done the electromagnetic and loss analyses. And J.C. has done the equivalent process of the material thermal conductivity.

Funding: This research was funded by National Natural Science Foundation of China (51577007) and Fundamental Research Funds for the Central Universities (2015RC016).

Conflicts of Interest: The authors declare no conflict of interest.

References

1. Baik, S.K.; Kwon, Y.K.; Kim, H.M.; Kim, S.H.; Lee, J.D.; Kim, Y.C.; Park, H.J.; Kwon, W.S.; Park, G.S. Electrical Parameter Evaluation of a 1MW HTS Motor Via Analysis and Experiments. *Cryogenics* **2009**, *49*, 271–276. [CrossRef]
2. Kwon, Y.K.; Kim, H.M.; Baik, S.K.; Lee, E.Y.; Lee, J.D.; Kim, Y.C.; Lee, S.H.; Hong, J.P.; Jo, Y.S.; Ryu, K.S. Performance Test of a 1MW Class HTS Synchronous Motor for Industrial Application. *Phys. C Supercond.* **2008**, *468*, 2081–2086. [CrossRef]
3. Baik, S.; Kwon, Y. Electrical Design of a 17 MW Class HTS Motor for Ship Propulsion. *J. Supercond. Nov. Magn.* **2013**, *26*, 1283–1287. [CrossRef]
4. Kovalev, L.K.; Ilushin, K.V.; Penkin, V.T.; Kovalev, K.L.; Koneev, S.M.A.; Modestov, K.A.; Larionoff, S.A.; Gawalek, W.; Oswald, B. Electrical Machines with Bulk HTS Elements. *Phys. C Supercond.* **2001**, *357–360*, 860–865. [CrossRef]
5. Ji-Kwang, L.; Sang-Ho, P.; Yungil, K.; Seyeon, L.; Woo-Seok, K.; Kyeongdal, C.; Song-Yop, H. Electrical Properties Analysis and Test Result of Windings for a Fully Superconducting 10 Hp Homopolar Motor. *IEEE Trans. Appl. Supercond.* **2012**, *22*, 5201405. [CrossRef]
6. Yoshida, K.; Matsumoto, H. Electromagnetic Force Analysis of Hts Bulk in DC-Magnetic Fields Due to Electromagnet. *Phys. C Supercond.* **2002**, *378*, 848–852. [CrossRef]
7. Masson, P.J.; Tixador, P.; Ordonez, J.C.; Morega, A.M.; Luongo, C.A. Electro-Thermal Model for HTS Motor Design. *IEEE Trans. Appl. Supercond.* **2007**, *17*, 1529–1532. [CrossRef]
8. Nakamura, T.; Miyake, H.; Ogama, Y.; Morita, G.; Muta, I.; Hoshino, T. Fabrication and Characteristics of HTS Induction Motor by the Use of Bi-2223/Ag Squirrel-Cage Rotor. *IEEE Trans. Appl. Supercond.* **2006**, *16*, 1469–1472. [CrossRef]
9. Jin, J.; Zheng, L.H.; Guo, Y.G.; Zhu, J.G.; Grantham, C.; Sorrell, C.C.; Xu, W. High-Temperature Superconducting Linear Synchronous Motors Integrated with HTS Magnetic Levitation Components. *IEEE Trans. Appl. Supercond.* **2012**, *22*, 5202617.
10. Fang, J.; Sheng, L.; Li, D.; Zhao, J.; Li, S.; Qin, W.; Fan, Y.; Zheng, Q.L.; Zhang, W. Influence Analysis of Structural Parameters and Operating Parameters on Electromagnetic Properties of HTS Linear Induction Motor. *Phys. Procedia* **2012**, *27*, 408–411. [CrossRef]
11. Gamble, B.; Snitchler, G.; MacDonald, T. Full Power Test of a 36.5 MW HTS Propulsion Motor. *IEEE Trans. Appl. Supercond.* **2011**, *21*, 1083–1088. [CrossRef]
12. Huaming, W.; Bailey, W.; Goddard, K.; Al-Mosawi, M.; Beduz, C.; Yifeng, Y. Performance Test of a 100 kW HTS Generator Operating at 67 K-77 K. *IEEE Trans. Appl. Supercond.* **2009**, *19*, 1652–1655. [CrossRef]
13. Morita, G.; Nakamura, T.; Muta, I. Theoretical Analysis of a YBCO Squirrel-Cage Type Induction Motor Based on an Equivalent Circuit. *Supercond. Sci. Technol.* **2006**, *19*, 473–478. [CrossRef]
14. Sato, K.; Kumagai, M.; Ito, K.; Watanabe, Y.; Gocho, Y. An Approach to Optimal Thermal Design of Superconducting Generator Rotor. *IEEE Trans. Energy Convers.* **1986**, *EC-1*, 217–224. [CrossRef]
15. Kulkarni, D.P.; Rupertus, G.; Chen, E. Experimental Investigation of Contact Resistance for Water Cooled Jacket for Electric Motors and Generators. *IEEE Trans. Energy Convers.* **2012**, *27*, 204–210. [CrossRef]
16. Yen, F.; Li, J.; Zheng, S.J.; Liu, L.; Ma, G.T.; Wang, J.S.; Wang, S.Y.; Liu, W. A Single-Sided Linear Synchronous Motor with a High Temperature Superconducting Coil as the Excitation System. *Supercond. Sci. Technol.* **2010**, *23*, 105015. [CrossRef]
17. Li, W.; Han, J.; Huo, F.; Zhou, X.; Zhang, Y.; Li, Y. Influence of the End Ventilation Structure Change On the Temperature Distribution in the End Region of Large Water-Hydrogen-Hydrogen Cooled Turbogenerator. *IEEE Trans. Energy Convers.* **2013**, *28*, 278–288.
18. Ruan, L.; Gu, G.; Tian, X.; Yuan, J. The Comparison of Cooling Effect between Evaporative Cooling Method and Inner Water Cooling Method for the Large Hydro Generator. In Proceedings of the International Conference on Electrical Machines and Systems, Seoul, Korea, 8–11 October 2007; pp. 989–992.
19. Li, W.; Qiu, H.; Yi, R.; Zhang, X.; Li, L. Three-Dimensional Electromagnetic Field Calculation and Analysis of Axial-Radial Flux-Type High-Temperature Superconducting Synchronous Motor. *IEEE Trans. Appl. Supercond.* **2013**, *23*, 5200607. [CrossRef]

20. Sander, M.; Grilli, F. FEM-Calculations on the Frequency Dependence of Hysteretic Losses in Coated Conductors. *J. Phys. Conf. Ser.* **2010**, *234*, 022030. [CrossRef]
21. Zhao, Y.; Sorrell, C.C.; Cheng, C.H. Frequency Dependent Behavior of AC Loss in High Temperature Superconductors. *Phys. C Supercond. Its Appl.* **2001**, *357*, 614–616. [CrossRef]
22. Tsukamoto, O.; Li, Z. Ac Loss Characteristics of Bi2223/Ag Sheathed Tape Wires Subjected to Mechanical Strains and Stresses. *Supercond. Sci. Technol.* **2007**, *20*, S282–S292. [CrossRef]
23. Wang, Y.; Zhao, X.; Han, J.; Dai, S.; Xiao, L.; Lin, L. AC Losses and Mechanical Stability in 630 kV a Three-Phase HTS Transformer Windings. *Supercond. Sci. Technol.* **2007**, *20*, 463. [CrossRef]
24. Li, C.; Pei, Y.; Ni, R.; Cheng, S. Analysis of 3D Static Temperature Field of Water Cooling Induction Motor in Mini Electric Vehicle. In Proceedings of the International Conference on Electrical Machines and Systems (ICEMS), Beijing, China, 20–23 August 2011; pp. 1–5.
25. Li, W.; Song, C.; Li, L.; Cao, J. Electromagnetic analysis of axial-radial flux-type fully superconducting synchronous motor. In Proceedings of the CESS, New York, NY, USA, 30 May–1 June 2011; pp. 96–101. (In Chinese)
26. Sahin, F. Design and Development of a High-Speed Axial-Flux Permanent-Magnet Machine. Ph.D. Thesis, Technische Universiteit Eindhoven, Eindhoven, The Netherlands, 2001.
27. Madani, N. Design of a Permanent Magnet Synchronous Generator for a Vertical Axis Wind Turbine. Master's Thesis, Teknik Och Teknologier, Stockholm, Sweden, 2011.
28. Zanis, R.; Borisavljevic, A.; Jansen, J.W.; Lomonova, E.A. Iron Loss Investigation of Miniaturized Magnetic Gears Having Solid Cores. In Proceedings of the International Conference on Electrical Machines and Systems, Boston, MA, USA, 17–21 July 2014; pp. 3078–3082.
29. Li, W.; Cao, J.; Zhang, X. Electrothermal Analysis of Induction Motor with Compound Cage Rotor Used for Phev. *IEEE Trans. Ind. Electron.* **2010**, *57*, 660–668.
30. Xyptras, J.; Hatziathanassiou, V. Thermal Analysis of an Electrical Machine Taking Into Account the Iron Losses and the Deep-Bar Effect. *IEEE Trans. Energy Convers.* **1999**, *14*, 996–1003. [CrossRef]
31. Ball, K.S.; Farouk, B.; Dixit, V.C. An Experimental Study of Heat Transfer in a Vertical Annulus with a Rotating Inner Cylinder. *Int. J. Heat Mass Transf.* **1989**, *32*, 1517–1527. [CrossRef]
32. Hatziathanassiou, V.; Xypteras, J.; Archontoulakis, G. Electrical-Thermal Coupled Calculation of an Asynchronous Machine. *Arch. Elektrotech.* **1994**, *77*, 117–122. [CrossRef]
33. Wei, Y.; Meng, D.; Wen, J. *Heat Transfer Inner Electric Machines*; China Machine Press: Beijing China, 1998. (In Chinese)
34. Cao, J.; Li, W.; Cheng, S.; Zhang, X. Temperature Field Calculation and Associated Factor Analysis of Induction Motor with Compound Cage Rotor. In Proceedings of the CSEE, Dallas, TX, USA, 21 April 2008; pp. 96–103. (In Chinese)